7Li NMR Chemical Shift Imaging To Detect Microstructural Growth of Lithium in All-Solid-State Batteries

Lauren E. Marbella,[†,§,∥] Stefanie Zekoll,[‡,⊥,∥] Jitti Kasemchainan,[‡] Steffen P. Emge,[†] Peter G. Bruce,[‡,⊥] and Clare P. Grey*[†,⊥]

[†]Department of Chemistry, University of Cambridge, Lensfield Road, Cambridge CB2 1EW, U.K.

[‡]Department of Materials, University of Oxford, Parks Road, Oxford OX1 3PH, U.K.

[⊥]The Faraday Institution, Quad One, Harwell Science and Innovation Campus, Didcot, U.K.

S *Supporting Information*

ABSTRACT: All-solid-state batteries potentially offer safe, high-energy-density electrochemical energy storage, yet are plagued with issues surrounding Li microstructural growth and subsequent cell death. We use 7Li NMR chemical shift imaging and electron microscopy to track Li microstructural growth in the garnet-type solid electrolyte, $Li_{6.5}La_3Zr_{1.5}Ta_{0.5}O_{12}$. Here, we follow the early stages of Li microstructural growth during galvanostatic cycling, from the formation of Li on the electrode surface to dendritic Li connecting both electrodes in symmetrical cells, and correlate these changes with alterations observed in the voltage profiles during cycling and impedance measurements. During these experiments, we observe transformations at both the stripping and plating interfaces, indicating heterogeneities in both Li removal and deposition. At low current densities, 7Li magnetic resonance imaging detects the formation of Li microstructures in cells before short-circuits are observed and allows changes in the electrochemical profiles to be rationalized.
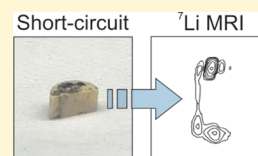
INTRODUCTION

All-solid-state batteries are one of the most promising technologies to improve safety and energy density of Li-based batteries.[1] To realize the high energy densities that are desirable for use in electric vehicles, Li-metal anodes are, however, required.[2,3] Although most solid electrolytes react with Li metal, garnet-type solid electrolytes such as $Li_7La_3Zr_2O_{12}$ (LLZO) show the highest stability against Li metal.[4,5] Doping LLZO with elements such as Al, Ta, and Ga can stabilize the high-conductivity cubic phase (10^{-4}–10^{-3} S/cm).[6−8]

Resonant ultrasound spectroscopy measurements have shown that doped cubic garnets, specifically $Li_{6.24}La_3Zr_2Al_{0.24}O_{11.98}$, exhibit high elastic (ca. 150 GPa) and shear (ca. 60 GPa) moduli.[9] According to the model developed by Monroe and Newman,[10] these mechanical properties should allow for the safe operation of Li metal, since dendrite suppression is predicted when the shear modulus of the electrolyte is twice that of Li (the shear modulus of Li is 4.2 GPa). Despite these favorable mechanical properties, short-circuiting events are still observed when Li−LLZO−Li symmetrical cells are cycled; it is still not clear whether dendrite formation is simply a function of current or whether it is associated with a critical current density under a given set of parameters.[11,12] This catastrophic cell failure is often the result of Li microstructural growth through the LLZO pellet/film that connects the two electrodes and leads to short-circuits.[13] A variety of mechanisms have been proposed to explain these results, including cation reduction and subsequent formation of metallic species at the Li−LLZO interface and LLZO grain boundaries,[14] inhomogeneous contact between LLZO solid electrolyte and Li electrodes,[12] and/or Li plating into crystallographic defects in the solid electrolyte that cause progressive particle cracking during cycling.[15] A variety of experimental techniques are required to test different theoretical models that describe how and why dendrites propagate through solid electrolytes.

Postmortem analysis of cycled Li−LLZO−Li symmetrical cells with microscopy techniques, such as scanning electron microscopy (SEM) and optical microscopy, requires precise cross-sectioning at the site of dendrite growth, which is often difficult and time-consuming, given that only a single dendrite may cause a short-circuit. If evidence of dendritic structures is found, definitive characterization of their presence with X-ray characterization strategies to determine elemental content (e.g., energy-dispersive X-ray spectroscopy (EDS)) is complicated by the presence of the multielement solid electrolyte and/or the low electron density of Li.[16] Despite this, Sakamoto and co-workers used a combination of SEM, EDS, and Auger electron spectroscopy (AES) to show that dendrites grow between the grains of LLZO, rather than through the particles.[16] In this work, the authors used Li KLL AES mapping to correlate the presence of Li-rich areas with the weblike structures observed in SEM and EDS. While Li enrichment is observed in the intergranular space, significant Li KLL AES signal arises from Li in LLZO itself in areas that are within the penetration depth of AES (approximately 5 nm). X-ray tomography, which unlike SEM/EDS is not destructive,

has shown success in visualizing porosity in solid electrolytes, providing insight into the correlation among fracturing, cell failure, and the observed critical current density.[17] However, Li metal cannot be readily distinguished from void space in the solid electrolyte in X-ray tomography because Li has a low attenuation coefficient (even when using high-energy, synchrotron X-ray sources). None of the aforementioned techniques have been used to probe the initial period of Li dendrite growth in all-solid-state batteries.

The lack of a routine, direct tool to diagnose Li dendrite growth has limited the correlation between short-circuiting events and Li microstructures, especially at the early stages of growth, and further investigation into the mechanisms (e.g., the role of interfacial resistance[18,19]) that contribute to cell death. Here, we show that ^{7}Li NMR chemical shift imaging (CSI) provides chemical and spatial information on Li microstructural growth in Li−LLZTO−Li symmetric cells (where LLZTO is Ta-doped LLZO). Ex situ ^{7}Li CSI measurements performed after applying different current densities indicate that ^{7}Li magnetic resonance imaging (MRI) is a useful tool to detect Li microstructural growth prior to the observation of obvious symptoms in the voltage profiles during galvanostatic cycling. Examination of cells at various states of charge shows inhomogeneities in both Li stripping and Li plating at a current density of 0.5 mA/cm^2, where the gradual accumulation of microstructural Li on the plating electrode causes sudden short-circuits from dendrites that connect the two electrodes and manifest as weblike structures in the postmortem SEM analysis.

■ EXPERIMENTAL SECTION

Materials and Synthesis of Ta-Doped LLZO. $Li_{6.5}La_3Zr_{1.5}Ta_{0.5}O_{12}$ was synthesized via a sol−gel method. Stochiometric amounts of Ta(V)Cl$_5$ (Sigma-Aldrich, 99.99%, 0.0028 mol), ZrO(NO$_3$)$_2$·1.8H$_2$O (Alfa Aesar, 99.9%, 0.00825 mol), La(III)(NO$_3$)$_3$·6H$_2$O (Sigma-Aldrich, 99.999%, 0.0165 mol), and LiNO$_3$ (Sigma-Aldrich, 99.99%, 0.03575 mol) were weighed out separately inside an Ar-filled glovebox (O$_2$ and H$_2$O levels below 0.1 ppm). A 20% weight excess of LiNO$_3$ was added to compensate for any Li losses during synthesis. Distilled H$_2$O was added to each vial to dissolve each of the Li, Zr, and La precursors, whereas 1.5 mL of dried ethanol was used to dissolve the Ta precursor. All of the dissolved precursors were then mixed together at a 1:1 molar ratio of ethylene glycol (Sigma-Aldrich, 99.8%, 0.05743 mol) and citric acid monohydrate (Sigma-Aldrich, ≥99.0%, 0.05743 mol) and topped with more distilled H$_2$O to obtain a 500 mL precursor solution. The precursor solution was first heated and stirred on a hot plate at 90−100 °C overnight, followed by 4 h of heating in an oven at 100 °C. The resulting gel was ground and further heated to 400 °C for 10 h using a ramping rate of 2 °C/min and a cooling rate of 10 °C/min to form a black powder. The black powder was ground and pressed into several 13 mm diameter and 10 mm thick pellets. The pellets were then placed in an Al crucible and calcined at 900 °C for 12 h at a ramping rate of 5 °C/min to obtain the cubic LLZO phase. The calcined pellets were removed from the furnace and transferred into a glovebox to cool down further.

To ensure a homogeneous grain size, the now white, calcined LLZTO was ball-milled using a Retsch EMax high-energy ball mill (2 × 50 mL zirconia grinding jars containing 21.5 g of 5 mm diameter zirconia balls, 1 g calcined LLZTO, and 1−2 mL solvent) for 1 h at 600 rpm with cyclohexane as a solvent. After evaporating the cyclohexane, the ball-milled LLZTO was pressed into 5 mm diameter pellets with a thickness of 2.5 mm using a uniaxial hydraulic press (Specac) at a load of 1 tonne. The pressed pellets were fully covered in LLZTO mother-powder (calcined LLZTO powder and 7.5% mass Li$_2$O mixed by 300 rpm ball milling for 1 h with cyclohexane as the

solvent) and inserted into a preheated furnace at 1250 °C for 10 min. The sintered LLZTO pellets were polished with a silicon carbide waterproof abrasive disk (Kemet, grade 400) inside the glovebox.

X-ray Diffraction (XRD). A Rigaku SmartLab X-ray diffractometer with a 3 kW rotating-anode X-ray generator, Cu Kα$_1$ radiation, and a Ge 220 monochromator was used to generate powder X-ray diffraction (XRD) patterns of the synthesized LLZTO at different stages of the synthesis procedure. The XRD patterns of the calcined Ta-doped powder, the calcined and ball-milled Ta-doped powder, and the sintered Ta-doped powder were collected and compared to the LLZO cubic phase reported in the literature.[20] The measurements were performed at room temperature and 2θ ranged from 10 to 70° using a step size of 0.01.

Electrochemical Measurements. Galvanostatic cycling of symmetrical LLZTO with Li was performed using Gamry Interface-1000 devices. Sintered LLZTO pellets with an average diameter of 4.5 mm and a thickness of 2.5 mm were polished as described above. A Li metal foil was scratched inside the glovebox to remove any oxidized species on the surface. The Li metal foil was then pre-pressed using a uniaxial hydraulic press at a load of 10 tonnes to achieve a Li metal sheet with a thickness of about 40 μm to avoid lateral expansion during cycling. Li metal disks of 1.7 mm diameter were cut out and hand-pressed onto both sides of a sintered Ta-doped LLZO pellet. The assembled Li−LLZTO−Li cell was then inserted between two Cu current collectors inside a custom-made pouch cell and sealed under vacuum. An external pressure of about 8 MPa was applied to the symmetrical cell by clamping the pouch cell between two plastic plates. Galvanostatic cycling was carried out at a constant current density of 0.2 and 0.5 mA/cm^2 for a maximum of 5 and 2 h, respectively, per charge or discharge at room temperature, which accounts for a capacity of 1.0 mAh/cm^2. Note that we use the terms charge and discharge to indicate a change in the direction of current flow; the first discharge corresponds to stripping Li from one electrode and plating Li on the opposite electrode. A rest time of 5 min was programmed between each change in current direction, and additional electrochemical impedance (alternating current EIS) measurements were performed after each charge and discharge step in a frequency range of 1 MHz to 0.1 Hz at a voltage perturbation of 10 mV. For the discharge-only experiments, a constant current of 0.5 mA/cm^2 was applied to the cells and cells were stopped at various times during the discharge.

Scanning Electron Microscopy (SEM) and Energy-Dispersive X-ray Spectroscopy (EDS). Pristine and cycled Li−LLZTO−Li cells were cross-sectioned using an ultrasonic cutter (Sonotec) with a tungsten carbide blade inside the glovebox. The cross-sectioned cells were mounted on a custom-made holder with Cu adhesive tape and transferred from the glovebox into a Zeiss Merlin scanning electron microscope using an air-sensitive transfer device (Gatan). The cross-sectioned cells were inspected at an acceleration voltage of 3 kV and probe current of 100 μA. EDS was performed within the Zeiss Merlin SEM using a built-in Oxford Instruments X-Max 150 silicon drift detector. Secondary electron images were acquired and EDS elemental mapping was performed at an acceleration voltage of up to 3 kV. The collected data were analyzed using the AZtec software package.

^{7}Li Chemical Shift Imaging. All ^{7}Li NMR and CSI experiments were performed on a Bruker Avance III 300 spectrometer operating at 7.05 T (^{7}Li frequency = 116.59 MHz) equipped with a MicWB40 probe and a Micro2.5 triple axis gradient system. All measurements were collected using a 10 mm ^{1}H/^{7}Li exchangeable radio frequency (rf) insert. ^{7}Li chemical shifts were externally referenced to 1.0 M LiCl$_{(aq)}$ at 0 ppm. Li−LLZTO−Li symmetrical cells (pristine cells and those stopped at various states of charge) were placed inside of an airtight J-Young NMR tube and sealed inside of an Ar-filled glovebox. Before inserting in the NMR probe, the symmetrical cells were positioned so that the Li electrodes were oriented perpendicular with respect to the external magnetic field, B_0. The cells were then centered in the NMR coil for excitation and detection.

^{7}Li CSI experiments were performed using a CSI single phase-encoded spatial dimension (in this case, z) reported previously
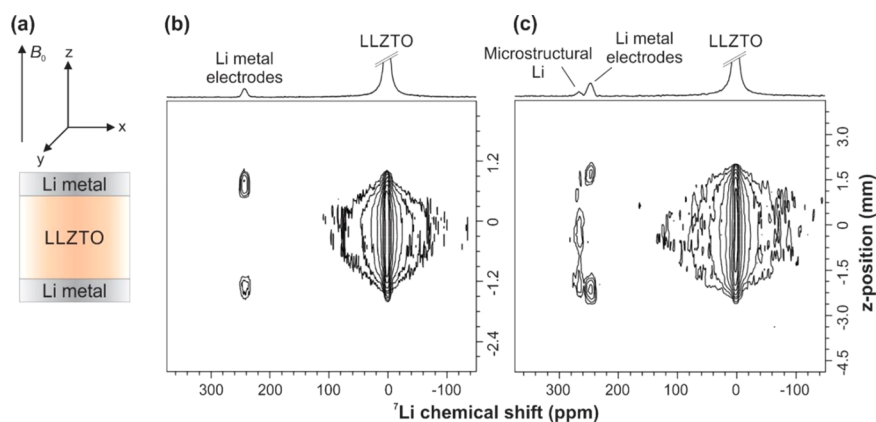
Figure 1. (a) Schematic of a symmetrical Li−LLZTO−Li cell depicting the orientation with respect to the external magnetic field, B_0, during the ^{7}Li CSI experiment. ^{7}Li chemical shift images of (b) pristine and (c) cycled Li−LLZTO−Li symmetrical cells. The ^{7}Li NMR signal of LLZTO is significantly more intense than that of Li metal and is truncated as indicated by hashes. The combination of the higher intensity and Lorentzian lineshape of the LLTZO resonance results in more visible noise in the baseline of this resonance in the two-dimensional spectra, as compared to that seen for Li metal. Galvanostatic cycling was performed at current densities of 0.2−1.0 mA/cm^2 to induce a short-circuit through the cell shown in (c) (Figure S2).
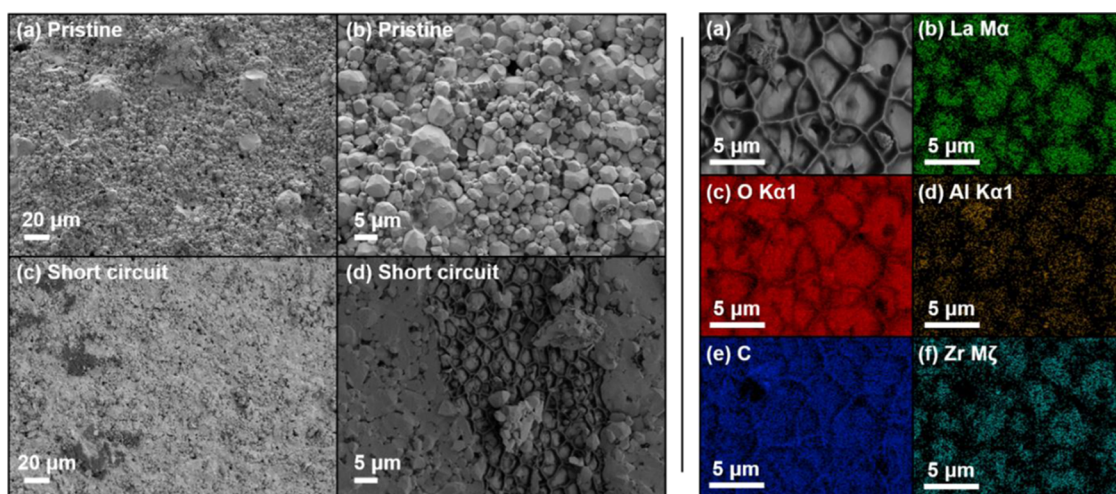

Figure 2. Left panel: scanning electron micrographs of (a, b) pristine and (c, d) short-circuited Li−LLZTO−Li cells at low (a, c) and high magnifications (b, d). In the short-circuited Li−LLZTO−Li cell, dark discolorations are observed that correspond to the weblike structures seen in the close-up image (d). Right panel: (a) SEM image of the weblike region and the corresponding EDS map for (b) La Mα, (c) O Kα$_1$, (d) Al Kα$_1$, (e) C, and (f) Zr Mζ of the Li−LLZTO−Li cell shown in (c) and (d) of the left panel.

(Figure S7).[21] Following the 90° rf pulse on the ^{7}Li channel, a phase-encoding gradient was applied along the z-axis that was stepped in 64 equal increments from −37.5 G/cm to +37.5 G/cm for 512−1024 transients with a recycle delay of 0.8 s. A total echo time of 700 μs was used with a field of view of 20 mm (nominal resolution of 300 μm).

RESULTS AND DISCUSSION

Ta-doped LLZO (Li$_{6.5}$La$_3$Zr$_{1.5}$Ta$_{0.5}$O$_{12}$, LLZTO) was synthesized via a sol−gel process. Powder XRD confirmed the successful synthesis of cubic LLZTO as the only crystalline phase (Figure S1). Ball-milled LLZTO powder was pressed into 5 mm diameter pellets with a thickness of approximately 2.5 mm, thick pellets being used to improve interpretation of data obtained from ^{7}Li CSI analysis where resolution is limited in the spatial dimension (approximately 300 μm for Li metal in the experiments reported here, but see discussion below). Symmetrical Li−LLZTO−Li cells were assembled by placing Li metal disks (diameter = 1.7 mm and thickness = 40 μm) on either side of LLZTO pellets (Figure 1a).

Figure 1b shows the ^{7}Li CSI of a pristine Li−LLZTO−Li cell; see the Supporting Information for a description of the ^{7}Li CSI experimental parameters. In the ^{7}Li chemical shift image, a one-dimensional (1D) ^{7}Li NMR spectrum is shown in the horizontal dimension, whereas the vertical dimension shows the corresponding MRI collected along the z-axis (slices are taken in the xy-plane from the bottom to the top in Figure 1). The MRI taken along the z-axis shows that LLZTO spans the length of the pellet, the Li metal electrodes capping either side. Although the spatial resolution of ^{7}Li CSI is an inherent limitation of this approach (e.g., the Li metal electrodes are approximately 40 μm in thickness, the thickness appears to be ~300 μm in the image, which is consistent with the nominal resolution of 300 μm used here), additional resolution is provided by coupling with the chemical specificity available in ^{7}Li NMR. High resolution between the electrodes and the solid electrolyte is evident by the large chemical shift difference between the regions corresponding to Li metal (244 ± 6 ppm) and LLZTO (1 ± 2 ppm).
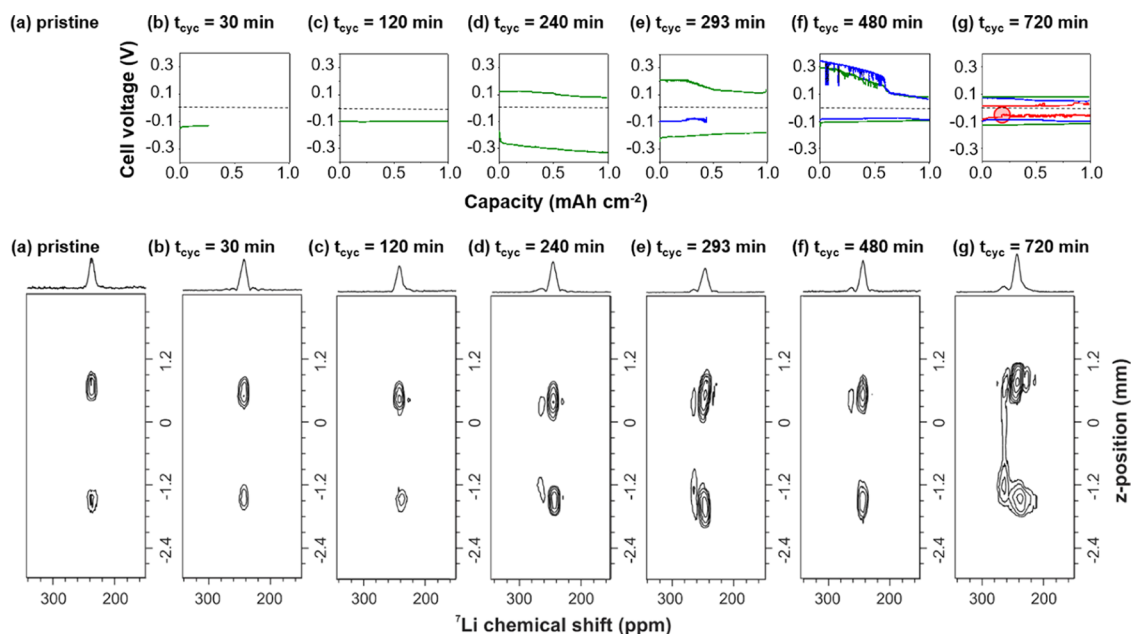
Figure 3. Galvanostatic cycling at 0.5 mA/cm² for a maximum of 2 h per discharge/charge (plating/stripping) (top) of Li−LLZTO−Li symmetrical cells stopped for ex situ analysis with ⁷Li CSI (bottom) for (a) pristine, (b) t_{cyc} = 30 min, (c) t_{cyc} = 120 min, (d) t_{cyc} = 240 min, (e) t_{cyc} = 293 min, (f) t_{cyc} = 480 min, and (g) t_{cyc} = 720 min. The first, second, and third cycles are shown in green, blue, and red, respectively. The short-circuit that occurred in (g) at 501 min is highlighted with a red circle. A detailed EIS analysis of all cells is shown in Table S2.

The Li−LLZTO−Li cell shown in Figure 1c was first cycled at a current of 0.2 mA/cm² and then to 1.0 mA/cm² until the voltage dropped close to 0 V, indicative of a short-circuit (Figure S2). Comparison of pristine and short-circuited cells with ⁷Li CSI shows the emergence of a new ⁷Li metal peak at 267 ± 6 ppm, which corresponds to microstructural Li. Due to bulk magnetic susceptibility effects, the chemical shift of Li metal is sensitive to changes in Li metal orientation with respect to the external magnetic field, B_0.[22] Since Li dendrites grow perpendicular to the Li metal electrodes, the signal from Li dendrites is distinct from that of the Li electrode[23] (Figures 1c and S6). Thus, within a single measurement, we are able to confirm the presence of Li microstructures that span the entire electrolyte region (Figure 1c) and correlate these structures with the short-circuiting event observed during cycling (Figure S2). The images shown in Figure 1c provide a measure of the concentration of Li dendrites/microstructures in the LLZTO pellet as a function of distance from the Li metal electrodes, but they do not identify the location of the dendrites in the xy-plane (the perpendicular direction). Figure S8 shows an image collected with the gradient applied along the y-axis (i.e., parallel to the Li metal electrodes) for the short-circuited cell shown in Figure 1c. The ⁷Li CSI image collected along the y-dimension indicates that the Li microstructural growth does not occur uniformly across the cell.

SEM analysis of Li−LLZTO−Li symmetrical cells that showed evidence of short-circuit during cycling displayed a weblike pattern when sectioned along a suspected dendrite region (Figure 2d, left panel). EDS of the weblike area showed a depletion of La, Al, and Zr in the intergranular space (Figure 2, right panel), consistent with intergranular Li dendrite growth.[16] Comparison of the pristine (Figure 2a,2b, left panel) and cycled cells with SEM and EDS indicates that these regions of elemental depletion and weblike structures are not present in the pristine material, suggesting that these features may be attributed to Li microstructures. However, cells

examined with SEM/EDS are not always cross-sectioned at the exact location of dendrite growth, making definitive proof of microstructural formation more accessible by ⁷Li CSI. Furthermore, the SEM analysis is destructive and non-quantitative.

Once we had established that we could detect the formation of Li microstructures after cell failure in all-solid-state batteries with MRI, we examined the utility of ⁷Li CSI to probe the initial stages of dendrite growth. Here, thicker pellets were used to clearly distinguish the presence of microstructures at different areas in the battery (e.g., near the surface of the electrode vs in the center of the electrolyte) in the imaging direction (z) during the MRI experiment. An important parameter that influenced cell failure was pellet thickness; thicker pellets took longer to short-circuit than thin pellets (Figure S3). For the ex situ experiments described here, solid electrolyte pellets from the same batch of LLZTO with the same thickness (2.46 ± 0.16 mm, where the error represents the standard deviation) were produced to extract qualitative trends in Li microstructural growth as a function of cycling time. Table S1 compiles the densities and ionic conductivities of all of the pellets, which vary from 85 to 90% and (0.55 to 1.4) × 10⁻³ S/cm, respectively. Li−LLZTO−Li symmetric cells were stopped at various time points during cycling at 0.5 mA/cm² (Figure 3), a current density at which cells reproducibly short-circuit in our laboratory, allowing us to monitor the processes that occur early on during the microstructural growth of Li. A total of 1.0 mAh/cm² of charge was passed in one direction, before reversing the direction (i.e., sign) of the current. Cells were stopped at cycling times of 30, 120, 240, 293, 480, and 720 min (Figure 3). Impedance measurements were taken before cycling and at specific time points during cycling (mainly between switches of current direction, Table S2). At early time points and before the current direction was reversed (t_{cyc} = 30 and 120 min, cell thicknesses = 2.49 and 2.52 mm, respectively), stable voltage

plateaus are observed (Figure 3b,c), and the ^{7}Li CSIs resemble those of the pristine cell (Figure 3a), indicating that little to no microstructural Li has formed. No significant changes in total impedance from EIS before and after cycling were observed (Table S2). After one complete cycle (t_{cyc} = 240 min, cell thickness = 2.22 mm), minor sloping is seen in the voltage profile that is coincident with the emergence of microstructural Li in the ^{7}Li CSI (Figure 3d). The corresponding ^{7}Li CSI shows ^{7}Li NMR shifts consistent with dense microstructural Li[24] at 264 ± 4 ppm. Based on the z-image, these Li microstructures are localized close to the electrode surface and are not yet detrimental to the cell (Figure 3d).

Despite the obvious resolution limitation in the spatial dimension, we can still estimate the depth that Li microstructures have penetrated into the solid electrolyte by measuring from the center of the two peaks (i.e., center of mass of the resonance) into the solid electrolyte along the z-position. We find that microstructural Li is found ~68 μm away from the top electrode and ~175 μm away from the bottom electrode after t_{cyc} = 240 min (Figure 3d). After t_{cyc} = 293 min, microstructural Li (^{7}Li shift 258 ± 3 ppm) appears to have penetrated further into the solid electrolyte, approximately 125 and 260 μm into the solid electrolyte (Figure 3e) from the top and bottom, respectively, and fluctuations in the voltage curves have become more dramatic. The Li−LLZTO−Li cell cycled for 480 min shows Li microstructures with a similar ^{7}Li shift (266 ± 3 ppm), but these signals are less intense and are localized closer to the electrode surface, extending only approximately 70 μm away from the electrode surface (Figure 3f). Variations in microstructure as a function of cycling time may be due to small variations in pellet thickness and pellet densification (the pellets used for t_{cyc} = 293 and 480 min are 2.65 and 2.44 mm thick, respectively) but are also dependent on the initial direction in which the current is passed. Repeating the experiment for t_{cyc} = 480 min on a separate pellet and marking the direction in which stripping and plating took place revealed that the electrode that first plates Li exhibits microstructural Li that penetrates more deeply into the LLZTO (Figure S9).

EIS measurements of the cell shown in Figure 3f (t_{cyc} = 480 min, Table S2 and Figure S4a) show that after the first discharge, the total impedance of the cell decreases significantly on the first plating/stripping "discharge" (as also observed in the cells shown in Figure 3b−d), which is explained at least in part by the formation of a better contact between the LLZTO pellet and the Li metal plating electrode, with the freshly plated Li diffusing directly out of the LLZTO particles. However, upon charging the cell, the total impedance increases significantly, with the interfacial resistance increasing the most. One source of the increase in interfacial resistance on charging is likely the removal of this freshly plated or deposited Li, removing the bridges or contacts between the LLZTO pellets and Li metal anode. This behavior is repeated in the second cycle with a decrease in the total impedance seen on discharge (in agreement with the stable cell voltage measured in this current direction) and the subsequent increase in the total impedance and interfacial resistance on charge. The steady decrease in overall bulk resistance is ascribed to the continued growth of dense Li microstructures that increasingly permeate into the pellet and that are clearly seen by MRI. Soft shorts (voltage spikes) are observed during charge at t_{cyc} = 480 min (Figure 3f) that are then followed by relatively normal battery operation during discharge. The lack of any significant

Li metal intensity connecting the Li metal electrodes in the CSI is consistent with the assignment of these voltage spikes to fine (i.e., low mass) Li dendrites that fuse (i.e., break) due to Li metal melting.[25]

Finally, at t_{cyc} = 720 min (cell thickness = 2.68 mm), a sharp voltage drop is observed at 501 min. When evaluated with ^{7}Li CSI at the end of this cycle, we observe a ^{7}Li resonance at 267 ± 7 ppm that completely penetrates the solid electrolyte, connecting the two electrodes (Figure 3g). The EIS measurements of this pellet after each switch in current direction again reveal an initial decrease in the total impedance upon the first discharge, followed by a marginal increase in total impedance upon the first charge. As more charge is passed through the cell, the total impedance is further lowered until 480 min into cycling, where the interfacial resistance suddenly increases significantly, shortly after which the cell short-circuits. This noticeable increase in interfacial resistance before short-circuiting requires further investigation but could potentially be used as an additional diagnostic tool in further studies.

Overall, this time series performed at a current density of 0.5 mA/cm^2 shows that dense Li microstructures observed in ^{7}Li CSI form early on and lead to Li microstructures that continue to penetrate the LLZTO matrix until they have connected both electrodes, causing a short-circuit and resulting in cell failure. This initial formation of dense Li microstructures is difficult to observe quantitatively from the voltage profiles or EIS measurements alone, but is a key intermediate in Li dendrite formation.

The variations in voltage profiles and Li microstructural growth at 0.5 mA/cm^2 in Figure 3, especially at the beginning of cycling, led us to re-examine the behavior of our cells at lower current densities. When Li−LLZTO−Li cells were cycled at 0.2 mA/cm^2 for >40 cycles, no evidence of any short-circuiting was seen in the voltage profile (Figure 4a). However,
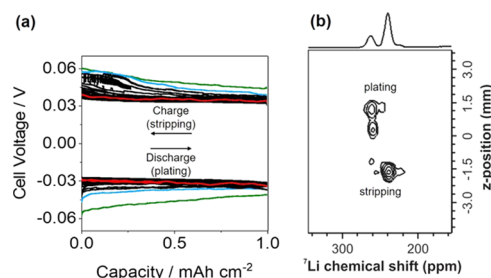

Figure 4. (a) Galvanostatic cycling at 0.2 mA/cm^2 for a maximum of 5 h per charge/discharge with the 1st cycle shown in green, 2nd cycle in light blue, and 40th cycle and 41st discharge (up to ~0.4 mAh/cm^2) in red. (b) Corresponding ^{7}Li CSI at the end of cycling showing the build-up of Li microstructures on the plating electrode (top).

inspection of the same sample with ^{7}Li CSI indicates that Li microstructural growth is persistent and is accumulating near the electrode surface (Figure 4b). Upon closer inspection (Figure 4a), we find that the voltage (overpotential) decreases with each cycle number, which may be related to the growth of microstructural Li into the solid electrolyte and thus a reduction of the distance between the two electrodes. The EIS measurements after each cycle confirm a continuous decrease in the total resistance of the cell with cycle number (Table S3). These experiments indicate that MRI may be a useful tool to detect Li microstructures before they are
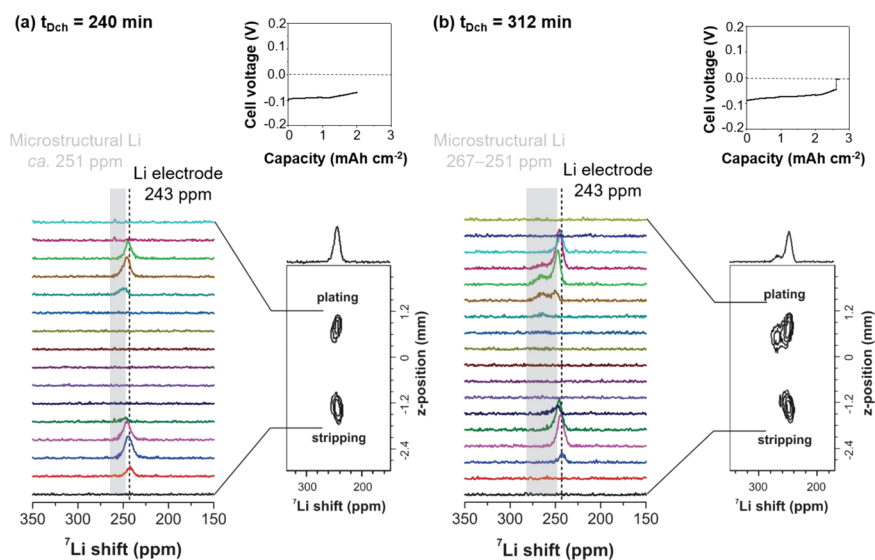
Figure 5. Constant plating at 0.5 mA/cm² of Li−LLZTO−Li symmetrical cells stopped for ex situ analysis with ⁷Li CSI at (a) t_{Dch} = 240 min and (b) t_{Dch} = 312 min. One-dimensional ⁷Li NMR spectra as a function of z-position in ⁷Li MRI are shown to the left of each ⁷Li CSI. The ⁷Li chemical shift corresponding to the Li metal electrode is shown at 243 ppm (dotted black line), as well as the region corresponding to Li microstructures (gray shading). Short-circuiting is evident in the voltage profile in (b) and is correlated with the Li dendrites observed in ⁷Li CSI at approx. 267 ppm. The plating (positive) and stripping (negative) electrodes are labeled in the image.

detrimental to the cell and correlate them with observed electrochemical parameters (e.g., voltage and impedance).

To provide further insight into the initial stripping/plating events and subsequent inhomogeneities in the stripping/plating, we performed constant plating experiments at a current density of 0.5 mA/cm². In these experiments, current is only passed in one direction to directly monitor the accumulation of microstructural Li on the positive (plating) electrode. From the experiments shown in Figure 3, we know that at early times (t_{Dch} = 30 and 120 min, current passed in only one direction), no microstructures are observed by ⁷Li CSI. At t_{Dch} = 240 min of current passing in one direction (thickness = 2.49 mm), evidence of high-density Li microstructures on both the positive (plating) and the negative (stripping) electrodes is observed (⁷Li shift of approximately 251 ppm, Figure 5a). The observation of dense Li microstructures in ⁷Li CSI occurs simultaneously with fluctuations in the voltage profile (Figure 5a), consistent with the trends observed in galvanostatic cycling experiments (Figure 3d−g). By comparing the 1D ⁷Li NMR spectra as a function of z-position in ⁷Li MRI (Figure 5a), the ⁷Li NMR shift at the electrode−electrolyte interface is shifted to higher frequency (approx. 251 ppm for the plating electrode and approx. 247 ppm for the stripping electrode) from that of the Li metal electrode (approx. 243 ppm).

Microstructural Li on the plating electrode is consistent with the uneven Li deposition that has been observed in liquid electrolytes.[24] However, the simultaneous presence of Li microstructures on the stripping electrode is surprising and indicates that Li removal from the negative electrode is also irregular. Roughening of Li at both stripping and plating electrodes is consistent with the work by Tsai et al.,[12] in which high interfacial resistance was found between Li metal and LLZO. The authors found that despite efforts to improve contact, an inhomogeneous contact between LLZO and Li metal resulted in "point contacts" that experience higher current densities than the initially applied current density during cycling. We hypothesize that these point contacts may

serve as nucleation sites for Li deposition/dissolution and can produce irregular surfaces and porosity on both the stripping and plating electrodes. Once formed, the roughened Li causes further deterioration at the Li metal/LLZO interface and likely creates hot spots or inhomogeneous removal (stripping) of Li from the Li anode, which presumably also becomes more porous/uneven.

After passing current (0.5 mA/cm²) in one direction for 312 min, a short-circuit is observed in the voltage profile (Figure 5b). Similarly, microstructural Li is present on both the stripping and plating electrodes, albeit with different ⁷Li resonances. The Li microstructures observed on the stripping electrode resonate at approximately 248 ppm, which is similar to the shifts observed at t_{Dch} = 240 min. Conversely, on the plating electrode, two ⁷Li resonances that correspond to microstructural Li in LLZTO are observed at ca. 251 and 267 ppm. The latter ⁷Li resonance is similar to that of the dendritic morphologies that are responsible for cell failure in this study (Figure 3g) as well as liquid electrolytes.[24] However, we note that no ⁷Li MRI signal is seen connecting the two electrodes, indicating that the structure that caused the short-circuit is below the detection limit of the NMR measurement (e.g., only a single dendrite is needed to short-circuit the battery and is too thin to be observed here with the current CSI parameters used).

■ CONCLUSIONS

Overall, we show that ⁷Li CSI is a powerful tool to monitor Li microstructural growth in all-solid-state batteries, particularly at the initial stages of dendrite growth that can be combined with higher spatial resolution (e.g., X-ray based) techniques. Using ⁷Li CSI, we have been able to attribute inhomogeneous Li stripping/plating in Li−LLZTO−Li cells to the microstructural Li that ultimately leads to dendrite growth with increasing cycle time. Dense Li microstructures that grow into the pellets are seen before any short-circuits are observed in the voltage profiles during electrochemical measurements, even when using low current densities of <0.5 mA/cm². From here,

it will be important to move to thinner all-solid-state batteries to understand the impact of pellet thickness and ionic transport on Li dendrite growth. Cell death due to short-circuit in Li−LLZTO−Li symmetric cells is clearly correlated with Li dendrites in [7]Li chemical shift images, an approach that can be extended to in situ/operando studies to explore the factors that dictate dendrite growth in solid electrolytes further.

■ ASSOCIATED CONTENT

Ⓢ Supporting Information

The Supporting Information is available free of charge on the ACS Publications website at DOI: 10.1021/acs.chemmater.8b04875. Supporting research data has been deposited and is available in the Cambridge data repository under DOI: 10.17863/CAM.38208 and the Oxford Research Archive under DOI: 10.5287/bodleian:0Nb1YzzxM.

Additional electrochemical measurements, XRD, ^{7}Li NMR, and [7]Li CSI data (PDF)

■ AUTHOR INFORMATION

Corresponding Author
*E-mail: cpg27@cam.ac.uk.

ORCID Ⓞ
Lauren E. Marbella: 0000-0003-1639-3913
Steffen P. Emge: 0000-0001-8613-9465
Clare P. Grey: 0000-0001-5572-192X

Present Address
§Department of Chemical Engineering, Columbia University, 500 W 120th Street, New York, New York 10027, United States (L.E.M.).

Author Contributions
‖L.E.M. and S.Z. contributed equally to this work.

Notes
The authors declare no competing financial interest.

■ REFERENCES

(1) Janek, J.; Zeier, W. G. A solid future for battery development. *Nat. Energy* **2016**, *1*, No. 16141.

(2) Cheng, X.-B.; Zhang, R.; Zhao, C.-Z.; Zhang, Q. Toward Safe Lithium Metal Anode in Rechargeable Batteries: A Review. *Chem. Rev.* **2017**, *117*, 10403−10473.

(3) Lin, D.; Liu, Y.; Cui, Y. Reviving the lithium metal anode for high-energy batteries. *Nat. Nanotechnol.* **2017**, *12*, 194.

(4) Kim, Y.; Yoo, A.; Schmidt, R.; Sharafi, A.; Lee, H.; Wolfenstine, J.; Sakamoto, J. Electrochemical Stability of $Li_{6.5}La_3Zr_{1.5}M_{0.5}O_{12}$ (M = Nb or Ta) against Metallic Lithium. *Front. Energy Res.* **2016**, *4*, 20.

(5) Zhu, Y.; He, X.; Mo, Y. Origin of Outstanding Stability in the Lithium Solid Electrolyte Materials: Insights from Thermodynamic Analyses Based on First-Principles Calculations. *ACS Appl. Mater. Interfaces* **2015**, *7*, 23685−23693.

(6) Allen, J. L.; Wolfenstine, J.; Rangasamy, E.; Sakamoto, J. Effect of substitution (Ta, Al, Ga) on the conductivity of $Li_7La_3Zr_2O_{12}$. *J. Power Sources* **2012**, *206*, 315−319.

(7) Rangasamy, E.; Wolfenstine, J.; Sakamoto, J. The role of Al and Li concentration on the formation of cubic garnet solid electrolyte of nominal composition $Li_7La_3Zr_2O_{12}$. *Solid State Ionics* **2012**, *206*, 28−32.

(8) Wolfenstine, J.; Ratchford, J.; Rangasamy, E.; Sakamoto, J.; Allen, J. L. Synthesis and high Li-ion conductivity of Ga-stabilized cubic $Li_7La_3Zr_2O_{12}$. *Mater. Chem. Phys.* **2012**, *134*, 571−575.

(9) Ni, J. E.; Case, E. D.; Sakamoto, J. S.; Rangasamy, E.; Wolfenstine, J. B. Room temperature elastic moduli and Vickers hardness of hot-pressed LLZO cubic garnet. *J. Mater. Sci.* **2012**, *47*, 7978−7985.

(10) Monroe, C.; Newman, J. The Impact of Elastic Deformation on Deposition Kinetics at Lithium/Polymer Interfaces. *J. Electrochem. Soc.* **2005**, *152*, A396−A404.

(11) Basappa, R. H.; Ito, T.; Morimura, T.; Bekarevich, R.; Mitsuishi, K.; Yamada, H. Grain boundary modification to suppress lithium penetration through garnet-type solid electrolyte. *J. Power Sources* **2017**, *363*, 145−152.

(12) Tsai, C.-L.; Roddatis, V.; Chandran, C. V.; Ma, Q.; Uhlenbruck, S.; Bram, M.; Heitjans, P.; Guillon, O. $Li_7La_3Zr_2O_{12}$ Interface Modification for Li Dendrite Prevention. *ACS Appl. Mater. Interfaces* **2016**, *8*, 10617−10626.

(13) Sharafi, A.; Meyer, H. M.; Nanda, J.; Wolfenstine, J.; Sakamoto, J. Characterizing the Li−$Li_7La_3Zr_2O_{12}$ interface stability and kinetics as a function of temperature and current density. *J. Power Sources* **2016**, *302*, 135−139.

(14) Fudong, H.; Yizhou, Z.; Xingfeng, H.; Yifei, M.; Chunsheng, W. Electrochemical Stability of $Li_{10}GeP_2S_{12}$ and $Li_7La_3Zr_2O_{12}$ Solid Electrolytes. *Adv. Energy Mater.* **2016**, *6*, No. 1501590.

(15) Porz, L.; Swamy, T.; Sheldon Brian, W.; Rettenwander, D.; Frömling, T.; Thaman Henry, L.; Berendts, S.; Uecker, R.; Carter, W. C.; Chiang, Y. M. Mechanism of Lithium Metal Penetration through Inorganic Solid Electrolytes. *Adv. Energy Mater.* **2017**, *7*, No. 1701003.

(16) Cheng, E. J.; Sharafi, A.; Sakamoto, J. Intergranular Li metal propagation through polycrystalline $Li_{6.25}Al_{0.25}La_3Zr_2O_{12}$ ceramic electrolyte. *Electrochim. Acta* **2017**, *223*, 85−91.

(17) Shen, F.; Dixit, M. B.; Xiao, X.; Hatzell, K. B. Effect of Pore Connectivity on Li Dendrite Propagation within LLZO Electrolytes Observed with Synchrotron X-ray Tomography. *ACS Energy Lett.* **2018**, *3*, 1056−1061.

(18) Cheng, L.; Chen, W.; Kunz, M.; Persson, K.; Tamura, N.; Chen, G.; Doeff, M. Effect of Surface Microstructure on Electrochemical Performance of Garnet Solid Electrolytes. *ACS Appl. Mater. Interfaces* **2015**, *7*, 2073−2081.

(19) Ishiguro, K.; Nemori, H.; Sunahiro, S.; Nakata, Y.; Sudo, R.; Matsui, M.; Takeda, Y.; Yamamoto, O.; Imanishi, N. Ta-Doped $Li_7La_3Zr_2O_{12}$ for Water-Stable Lithium Electrode of Lithium-Air Batteries. *J. Electrochem. Soc.* **2014**, *161*, A668−A674.

(20) Thompson, T.; Sharafi, A.; Johannes Michelle, D.; Huq, A.; Allen Jan, L.; Wolfenstine, J.; Sakamoto, J. A Tale of Two Sites: On Defining the Carrier Concentration in Garnet-Based Ionic Conductors for Advanced Li Batteries. *Adv. Energy Mater.* **2015**, *5*, No. 1500096.

(21) Chang, H. J.; Ilott, A. J.; Trease, N. M.; Mohammadi, M.; Jerschow, A.; Grey, C. P. Correlating Microstructural Lithium Metal Growth with Electrolyte Salt Depletion in Lithium Batteries Using [7]Li MRI. *J. Am. Chem. Soc.* **2015**, *137*, 15209−15216.

(22) Trease, N. M.; Zhou, L.; Chang, H. J.; Zhu, B. Y.; Grey, C. P. In situ NMR of lithium ion batteries: Bulk susceptibility effects and practical considerations. *Solid State Nucl. Magn. Reson.* **2012**, *42*, 62−70.

(23) Chandrashekar, S.; Trease, N. M.; Chang, H. J.; Du, L.-S.; Grey, C. P.; Jerschow, A. [7]Li MRI of Li batteries reveals location of microstructural lithium. *Nat. Mater.* **2012**, *11*, 311.

(24) Chang, H. J.; Trease, N. M.; Ilott, A. J.; Zeng, D.; Du, L.-S.; Jerschow, A.; Grey, C. P. Investigating Li Microstructure Formation on Li Anodes for Lithium Batteries by in Situ ^{6}Li/^{7}Li NMR and SEM. *J. Phys. Chem. C* **2015**, *119*, 16443−16451.

(25) Abraham, K. M. Directions in secondary lithium battery research and development. *Electrochim. Acta* **1993**, *38*, 1233−1248.